Performance evaluation of coherent free space optical communications with a double-stage fast-steering-mirror adaptive optics system depending on the Greenwood frequency

Wei Liu,[1] Kainan Yao,[2] Danian Huang,[1,*] Xudong Lin,[2] Liang Wang,[2] and Yaowen Lv[3]

[1]*College of Geoexploration Science and Technology, Jilin University, 938, West Democracy Street, Changchun, Jilin 130026, China*

[2]*Changchun Institute of Optics, Fine Mechanics and Physics, Chinese Academy of Sciences, 3888, Nanhu Road, Changchun, Jilin 130033, China*

[3]*The School of Optoelectronic Engineering, Changchun University of Science and Technology, 7089 Weixing Road, Changchun, Jilin 130022, China*

[*]*professordn@163.com*

Abstract: The Greenwood frequency (GF) is influential in performance improvement for the coherent free space optical communications (CFSOC) system with a closed-loop adaptive optics (AO) unit. We analyze the impact of tilt and high-order aberrations on the mixing efficiency (ME) and bit-error-rate (BER) under different GF. The root-mean-square value (RMS) of the ME related to the RMS of the tilt aberrations, and the GF is derived to estimate the volatility of the ME. Furthermore, a numerical simulation is applied to verify the theoretical analysis, and an experimental correction system is designed with a double-stage fast-steering-mirror and a 97-element continuous surface deformable mirror. The conclusions of this paper provide a reference for designing the AO system for the CFSOC system.

OCIS codes: (060.0060) Fiber optics and optical communications; (010.1080) Active or adaptive optics; (010.1330) Atmospheric turbulence; (060.1660) Coherent communications.

References and links

1. A. García-Zambrana, R. Boluda-Ruiz, C. Castillo-Vázquez, and B. Castillo-Vázquez, "Transmit alternate laser selection with time diversity for FSO communications," Opt. Express **22**(20), 23861–23874 (2014).
2. J. Zhang, S. Ding, H. Zhai, and A. Dang, "Theoretical and experimental studies of polarization fluctuations over atmospheric turbulent channels for wireless optical communication systems," Opt. Express **22**(26), 32482–32488 (2014).
3. X. Ma, J. Sun, Y. Zhi, Y. Zhou, W. Lu, P. Hou, Q. Xu, and L. Liu, "Performance analysis of pupil-matching optical differential receivers in space-to-ground laser communication," Appl. Opt. **53**(14), 3010–3018 (2014).
4. J. Perez, S. Zvanovec, Z. Ghassemlooy, and W. O. Popoola, "Experimental characterization and mitigation of turbulence induced signal fades within an ad hoc FSO network," Opt. Express **22**(3), 3208–3218 (2014).
5. K. Yao, J. Wang, X. Liu, H. Li, M. Wang, B. Cui, and S. Yu, "Pyramid wavefront sensor using a sequential operation method," Appl. Opt. **54**(13), 3894–3901 (2015).
6. Y. Rahmat-Samii and A. C. Densmore, "Technology Trends and Challenges of Antennas for Satellite Communication Systems," IEEE Trans. Antenn. Propag. **03**, 1–14 (2014).
7. W. Liu, W. Shi, K. Yao, J. Cao, P. Wu, and X. Chi, "Fiber Coupling efficiency analysis of free space optical communication systems with holographic modal wave-front sensor," Opt. Laser Technol. **60**, 116–123 (2014).
8. W. Liu, W. Shi, B. Wang, K. Yao, Y. Lv, and J. Wang, "Free space optical communication performance analysis with focal plane based wavefront measurement," Opt. Commun. **309**, 212–220 (2013).
9. W. Liu, W. Shi, J. Cao, Y. Lv, S. Wang, J. Wang, and X. Chi, "Bit error rate analysis with real-time pointing errors correction in free space optical communication systems," Optik (Stuttg.) **125**(1), 324–328 (2014).
10. A. Belmonte, A. Rodríguez, F. Dios, and A. Comeón, "Phase compensation considerations on coherent, free-space laser communications system," Proc. SPIE **6736**, 67361A (2007).
11. A. Belmonte, "Influence of atmospheric phase compensation on optical heterodyne power measurements," Opt. Express **16**(9), 6756–6767 (2008).

#262563 Received 5 Apr 2016; revised 1 Jun 2016; accepted 2 Jun 2016; published 8 Jun 2016

12. M. Li and M. Cvijetic, "Coherent free space optics communications over the maritime atmosphere with use of adaptive optics for beam wavefront correction," Appl. Opt. **54**(6), 1453–1462 (2015).
13. J. Li, Z. Zhang, J. Gao, J. Sun, and W. Chen, "Bandwidth of adaptive optics system in atmospheric coherent laser communication," Opt. Commun. **359**, 254–260 (2016).
14. L. Zuo, Y. Ren, A. Dang, and G. Hong, "Performance of coherent BPSK systems using phase compensation and diversity techniques," in *Global Telecommunications Conference* (IEEE, 2010), pp. 1–5.
15. L. Zuo, A. Dang, Y. Ren, and H. Guo, "Performance of phase compensated coherent free space optical communications through non-Kolmogorov turbulence," Opt. Commun. **28**, 41491–41495 (2011).
16. H. Jian, D. Ke, L. Chao, Z. Peng, J. Dagang, and Y. Zhoushi, "Effectiveness of adaptive optics system in satellite-to-ground coherent optical communication," Opt. Express **22**(13), 16000–16007 (2014).
17. C. Liu, S. Chen, X. Li, and H. Xian, "Performance evaluation of adaptive optics for atmospheric coherent laser communications," Opt. Express **22**(13), 15554–15563 (2014).
18. C. Liu, M. Chen, S. Chen, and H. Xian, "Adaptive optics for the free-space coherent optical communications," Opt. Commun. **361**, 21–24 (2016).
19. J. Huang, H. Mei, K. Deng, L. Kang, W. Zhu, and Z. Yao, "Signal to noise ratio of free space homodyne coherent optical communication after adaptive optics compensation," Opt. Commun. **356**, 574–577 (2015).
20. N. Roddier, "Atmospheric wavefront simulation using Zernike polynomials," Opt. Eng. **29**(10), 1174–1180 (1990).
21. R. Changhui, J. Wenhan, L. Ning, T. Guomao, S. Feng, Z. Xuejun, and T. Huimin, "Temporal Correction Effectiveness of Adaptive Optical System for Light Wave Atmospheric Propagation," Acta Opt. Sin. **21**, 933–938 (2001).

1. Introduction

With higher spectral efficiency and data rate, the greater ability of decrease both background and thermal noise, and the more sensitivity coherent receiver, the performance of coherent detection scheme is more excellent comparable with the intensity modulation direct detection in the free space optical communications (FSOC) [1–4]. However, atmospheric turbulence is the development bottleneck for a coherent free space optical communications (CFSOC) system. The bit-error-rate (BER) and mixing efficiency (ME) of a CFSOC is severely degraded by turbulence-induced wavefront phase aberrations [5–9].

Much of the existing research focused on the performance analysis of the CFSOC based-on an adaptive optics (AO) unit. Aniceto Belmonte analyzed the capacity of CFSOC links using atmospheric compensation techniques and the influence of atmospheric phase compensation on optical heterodyne power measurements. The effects of various parameters are given, including the ratio of the receiver aperture diameter to the wavefront coherent diameter, the strength of the scintillation index, and the number of modes compensated. The results showed that the phase-compensated heterodyne receivers offered the potential for overcoming the limitations imposed by the atmosphere by the partial correction of turbulence-induced wavefront phase aberrations. However, wavefront amplitude fluctuations limited the compensation process and diminished the achievable heterodyne performance [10,11]. Ming Li et al. established a CFSOC channel model for maritime conditions, and a comprehensive comparison of performance was made between the maritime and terrestrial atmospheric links. The results showed that the BER of the CFSOC system can be significantly improved with AO unit [12]. Jiawei Li et al. performed the BER performance of CFSOC with binary phase shift keying (BPSK) modulation, the servo bandwidth was investigated using different values for the Greenwood frequency (GF), however the experimental analysis is ignored [13]. Zuo et al. used Zernike mode to investigate the BER performance of CFSOC system in weak non-Kolmogorov turbulence and showed that BER decreased sharply as more modes were corrected employing phase compensation techniques. The optimal compensation parameters are found showing that the CFSOC system can obtain the minimum BER. In addition, the mode is accurate with the large of the ratio of the receiving aperture diameter D to the coherent length r_0 (D/r_0) [14,15]. Chao Liu and Jian Huang et al. analyzed the ME and BER performance improvement of the CFSOC with AO by numerical simulation and the experimental data of a 1.8 m telescope with a 127-element AO system, under different D/r_0. The results showed that the AO technique had great potential to improve the performances of the CFSOC. Especially, they also indicated that the tilt aberrations account for about 87% of

#262563 Received 5 Apr 2016; revised 1 Jun 2016; accepted 2 Jun 2016; published 8 Jun 2016

the total aberrations from atmospheric turbulence, and a lower response bandwidth caused by a large tilt mirror stroke cannot compensate high-order aberrations [16–19]. Above all, much research is around the AO system under different atmospheric turbulence evaluated by D/r_0. The analysis depending on the GF is scarce.

In this paper, the relationship of the fluctuation of the arrival angle caused by tilt aberrations, wavefront distortions caused by high-order aberrations, and the GF is derived. Moreover, the ME and BER is analyzed under different GF. Secondly, the relationship between the root-mean-square (RMS) of the ME, the RMS of tilt aberrations, and the GF is derived to estimate the volatility of the ME. At last, an AO unit with a double-stage fast-steering-mirror (FSM) and a 97-element continuous surface deformable mirror (CSDM) is designed. The performance of CFSOC with and without the first-stage FSM, the double-stage FSM and the high-order aberrations correction under different GF is analyzed. The experimental results illustrate the relationship between the performance of CFSOC, the closed-loop control bandwidth (CLCB), and the GF. The conclusions of this paper can offer reference data to the design of the CFSOC based-on AO unit.

2. Theoretical analysis

The schematic diagram of CFSOC system with AO unit to compensate atmospheric turbulence is shown in Fig. 1. As transmitting terminal, the laser beam is emitted by laser point source, and it is modulated into laser carrier signal. At the receiving terminal, the received optical signal is mixed with laser signal from local oscillation (LO) to generate the intermediate frequency signal. Then, according to the intermediate frequency signal, proper demodulator is used. And the received signal can be further processed by digital signal processer. However, during the transmitting, laser beam is distorted by atmospheric turbulence, and its wavefront and amplitude are disturbed. Accordingly, atmospheric compensation is indispensable in CFSOC system. We introduce AO unit to CFSOC system which consists of the wavefront corrector, the wavefront controller and the wavefront sensor. The work cycle of AO unit is divided into three steps: firstly, the wavefront sensor measures the wavefront aberrations of the optical signal as the feedback signal. Secondly, according to the feedback signal, the wavefront controller controls the wavefront corrector. Finally, the wavefront corrector corrects the wavefront aberrations in real time. Thus, atmospheric turbulence is compensated and the quality of the optical signal is improved.

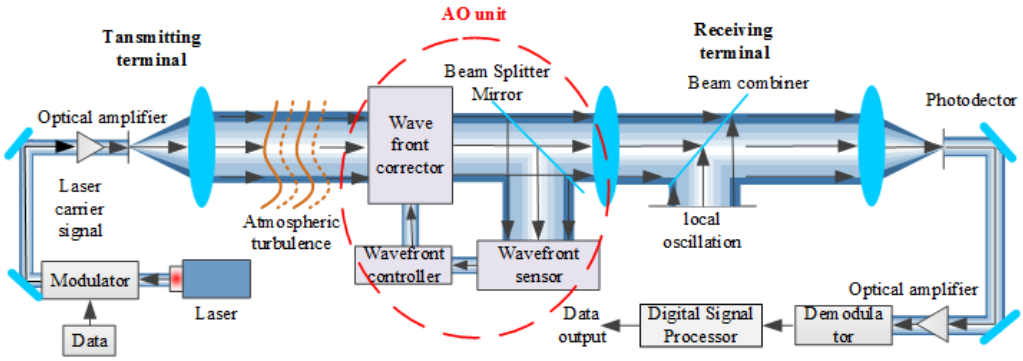

Fig. 1. The schematic diagram of the CFSOC system.

2.1 The ME of the CFSOC system

Assuming that the LO is a plane wave and the intensity of the optical signal is uniform, the optical field distributions of the optical signal and LO can be expressed as:

$$E_S = A_S E^{i(2\pi f_S t + \varphi_S)} \tag{1}$$

#262563 Received 5 Apr 2016; revised 1 Jun 2016; accepted 2 Jun 2016; published 8 Jun 2016

$$E_{LO} = A_O E^{i(2\pi f_O t + \varphi_O)} \tag{2}$$

where, A_s and A_o are the amplitudes of the optical signal and LO, respectively. f_s and f_o denote their frequencies, and φ_S and φ_O are the phases of the optical signal and LO, respectively.

According to the theory of coherent detection, the total optical power at a photodetector is given by:

$$I = \int_S (E_{LO} + E_S)(E_{LO} + E_S)^* ds \tag{3}$$

Substituting Eqs. (1) and (2) into Eq. (3), we can obtain as follows:

$$I = \int_S \left\{ A_O^2 + A_S^2 + 2A_O A_S \cos\left[2\pi(f_S - f_O) + \Delta\varphi\right] \right\} ds \tag{4}$$

where $\Delta\varphi = \varphi_S - \varphi_O$ denotes the phase difference between the optical signal and LO, and S is the area of the receiver aperture. In the Eq. (4), if $f_s = f_o$, it is called homodyne detection, and if $f_s \neq f_o$, it is called heterodyne detection. Since the symbol transmission rate is generally less than 1 ns in an FSOC system, the GF is in the millisecond orders of magnitude, and phase aberrations caused by atmospheric turbulence can be considered frozen during the detection time of every code, so $\Delta\varphi$ can be expressed by:

$$\Delta\varphi = \varphi(r) + \varphi(t) \tag{5}$$

where, $\varphi(r)$ is the time-independent phase aberrations caused by atmospheric turbulence, and $\varphi(t)$ is the modulated phase of the optical signal, it is space coordinate-independent.

The ME of the homodyne detection is defined by [17]:

$$\eta = \frac{[\int_S \mathrm{A_S A_O} \cos(\Delta\varphi) ds]^2}{\int_S \mathrm{A_S^2}\, ds \int_S \mathrm{A_O^2}\, ds} \tag{6}$$

2.2 The influence of wavefront aberrations on the ME

Because the tilt causes the major components of wavefront aberrations, we analyze the influence of the GF on the performance of tilt and high-order correction independently in this paper. That is to say, on the one hand, we derive the relationship of the ME, BER, and GF assuming the aberrations are all caused by tilt. On the other hand, the relationship is given considering the aberrations are entirely composed by high-order aberrations.

2.2.1 The influence of the tilt aberrations

In the CFSOC system, tilt aberrations, the major factor which degrades the ME [16], consist of two parts. One part contains the phase-locked error, which is expressed as phase delay of the optical signal and LO at the receiver. Another part is beam tilt caused by atmospheric turbulence and jitter of the acquisition tracking and pointing, which manifests as arrival angle fluctuations at the receiver [16]. We introduce the Zernike term to describe the wavefront aberrations, assuming the tilt aberrations are expressed by a direct-current term (Piston aberration) and tilt terms [20]. The direct-current term can be compensated by the phase-locked loop (PLL). Thus, in this paper, we only analyze the influence of the GF on arrival angle fluctuations of the optical signal caused by atmospheric turbulence. The variance of the arrival angle fluctuations is given by [21]:

$$\sigma_\beta^2 = 2.91 D^{-1/3} \int_0^L C_n^2(z) dz \tag{7}$$

#262563 Received 5 Apr 2016; revised 1 Jun 2016; accepted 2 Jun 2016; published 8 Jun 2016

where D denotes diameter of the receiver aperture, L is the transmission distance, and C_n^2 is the atmospheric refractive-index structure parameter. The GF describes the time-domain characteristic of atmospheric turbulence, it can be given by:

$$f_G = [0.10247k^2 v_{5/3} \sec\zeta]^{3/5} \tag{8}$$

where, f_G is the GF, ζ is the zenith angle, k is the wave number, $k = 2\pi/\lambda$, λ is the wavelength of the optical signal, $v_{5/3} = \int_0^L C_n^2(z)v(z)^{5/3}dz$, and $v(z)$ is the velocity. Both $C_n^2(z)$ and $v(z)$ are the functions of the transfer distance. $C_n^2(z)$ is influenced by the gradient of the atmospheric refractivity, which is dramatically changed with the altitude. Similarly, $v(z)$ also changes with the altitude. For the horizontal-path CFSOC system, $v(z)$ is considered as constant within a certain period of time. According to Eqs. (7) and (8), we can obtain:

$$\sigma_\beta^2 = \frac{28.4D^{-1/3} f_G^{5/3}}{k^2 v^{5/3} \sec\zeta} \tag{9}$$

Here, we assume that only tilt is considered. Generally, the arrival angle is less than 1 rad, the wavefront aberrations on the receiver aperture can be written as [16]:

$$\Delta\varphi = \varphi_{tilt} = \tan(\beta) r\cos\theta \approx \beta r\cos\theta \tag{10}$$

where r and θ are polar coordinate variables, φ_{tilt} is the tilt aberrations, and β is the arrival angle. We assume that the receiver is a homodyne detector, then the optical signal and LO are the plane wave of uniform intensity, and that the scintillation of the LO can be disregarded, the Eq. (6) can be simplified as [16]:

$$\begin{aligned} \eta_t &= \left[\frac{1}{S}\int_S \cos(\Delta\varphi)ds\right]^2 = \left[\frac{1}{S}\int_0^R\int_0^{2\pi} \cos(\beta r\cos\theta) r dr d\theta\right]^2 \\ &= \left[2\pi R^2 \frac{1}{S}\frac{J_1(kR\beta)}{kR\beta}\right]^2 = \left[\frac{2J_1(kR\beta)}{kR\beta}\right]^2 \end{aligned} \tag{11}$$

where η_t is the ME only considering tilt aberrations, J_1 is the first-order Bessel function of the first kind, and R is the radius of the aperture.

The relationship between the RMS value of the tilt aberrations and arrival angle can be written as [16]:

$$\sigma_{tilt} = \sqrt{\frac{1}{S}\int_0^R\int_0^{2\pi} (\beta r\cos\theta)^2 r dr d\theta} = \frac{kR\beta}{2} \tag{12}$$

Comparing the expression of ME with RMS of tilt aberrations, the ME is given by:

$$\eta_t = \left[\frac{2J_1(kR\beta)}{kR\beta}\right]^2 \tag{13}$$

Generally, the RMS value is often used to describe the volatility. According to the RMS computing method, the relationship between the RMS of the ME and the RMS of the tilt aberrations is given by:

$$\sigma_{\eta_t} = \sqrt{\{\frac{d\eta}{d\beta}\}^2 \sigma_\beta^2} = \frac{2J_2(kR\beta)}{\beta} \cdot \sqrt{\frac{28.4D^{-1/3} f_G^{5/3}}{k^2 v^{5/3} \sec\zeta}} = \frac{5.33D^{5/6} f_G^{5/6} J_2(2\sigma_{tilt})}{2\sigma_{tilt} v^{5/6} \sec^{1/2}\zeta} \tag{14}$$

#262563 Received 5 Apr 2016; revised 1 Jun 2016; accepted 2 Jun 2016; published 8 Jun 2016

According to Eqs. (9) and (14), the arrival angle and the fluctuation of the ME are related to the GF.

As indicated in the preceding analysis, the influence of the GF on the fluctuation of the arrival angle caused by the tilt aberrations is analyzed. In addition, the relationship between the RMS of the ME, the RMS of the tilt aberrations, and the GF is given.

2.2.2 The influence of the high-order aberrations

For the CFSOC system, the phase fluctuation in time domain and space domain both degrade the CFSOC performance. Usually, the phase fluctuation in time domain can be reduced by PLL, and the AO unit is used to overcome the phase fluctuation in the space domain.

Similar to the previous analysis, assuming the optical signal and LO obey uniform distributions at the coherent plane, the ME of the homodyne detection can be expressed:

$$\eta_c = [\frac{1}{S}\int_S \cos(\Delta\varphi)ds]^2 \tag{15}$$

where η_c is the ME. Assuming the aberrations are all composed of high-order component, the RMS of the residual aberrations is less than 1 rad, according to the Taylor series expansion we obtain [16]:

$$\eta_c = \{\frac{1}{S}\int_S [1-\frac{\varphi^2(r)}{2}]ds\}^2 = (1-\frac{\sigma_\varphi^2}{2})^2 \tag{16}$$

where σ_φ^2 is the RMS of the optical signal high-order aberrations (excluding Piston and tilt aberrations).

The AO system is considered as an effective way to correct high-order wavefront aberrations. We analyze the performance of a CFSOC system with an AO unit under different GF. The RMS of the residual wavefront aberrations after AO correction based on a CSDM can be given by [21]:

$$\sigma_\varphi = \left[\alpha_F(\frac{d}{r_0})^{5/3} + \kappa(\frac{f_G}{f_{3dB}})^{5/3}\right]^{1/2} (rad) \tag{17}$$

where α_F is the fitting error coefficient, d is the equivalent distance between the actuators on the entrance pupil of the receiving antenna, r_0 is atmospheric coherence length, f_{3dB} is the CLCB, and κ is a constant. For the plane wave, κ = 1. When the GF is zero, Eq. (17) can be given by:

$$\sigma_{\varphi_0} = \left[\alpha_F(\frac{d}{r_0})^{5/3}\right]^{1/2} (rad) \tag{18}$$

According to Kolmogorov theory, the Eq. (18) meets the relationship of the RMS of wavefront aberrations and atmospheric coherence length in an inertial subinterval, under the condition of partially-homogeneous and isotropy [9]. Assuming the residual aberrations after correction are less than 1 rad, substituting Eq. (17) into Eq. (16), the ME of the CFSOC with an AO unit is given by:

$$\eta_c = (1-\frac{\sigma_\varphi^2}{2})^2 = \{1-\left[\alpha_F(\frac{d}{r_0})^{5/3} + \kappa(\frac{f_G}{f_{3dB}})^{5/3}\right]/2\}^2 \tag{19}$$

Hence, according to Eq. (19), the influence of the GF on the ME can be analyzed under different CLCB.

#262563 Received 5 Apr 2016; revised 1 Jun 2016; accepted 2 Jun 2016; published 8 Jun 2016

2.3 The BER of the CFSOC system

In the coherent detection system, BER is given by:

$$BER = \frac{1}{2} erfc(\frac{Q}{\sqrt{2}}) \tag{20}$$

where *erfc* is the complementary error function, and $Q = \sqrt{SNR}$, where *SNR* is the signal to noise ratio of homodyne detection. For the synchronous BPSK received system, the optical power at the receive terminal is given by:

$$P_S = N_P h\nu B \tag{21}$$

The *SNR* without atmospheric turbulence is given by:

$$SNR_0 = \frac{2\delta P_S}{h\nu B} = 2\delta N_P \tag{22}$$

where N_p is the number of photons received within a single bit, and δ is the quantum efficiency of the detector. The BER of the homodyne receiver is:

$$BER = \frac{1}{2} erfc\left(\sqrt{2\delta N_P \eta}\right) \tag{23}$$

3. Numerical simulation

We assume the modulation is BPSK with the bit-rate of 2Gbps and the receiver is the homodyne detection scheme, and the intensity on the coherent plane is uniform. Considering horizontal-path transmission, the fluctuation of wind velocity is ignored. In the following numerical simulation, we show the curve of the angle fluctuations with the GF. And the relationship between the RMS of the ME and tilt aberrations under the different GF is given. Then the impact of the CLCB of AO unit on the ME is analyzed when the aberrations are composed of the high-order component. The relationship between the CLCB and the BER is given at last. In our simulation, the laser wavelength is 1550 nm, the receiving antenna aperture is 1.2 m, the zenith angle is nearly 90°, and the GF is from 50 Hz to 160 Hz. According to Eq. (9), the curve of the arrival angle fluctuation versus GF is shown in Fig. 2.

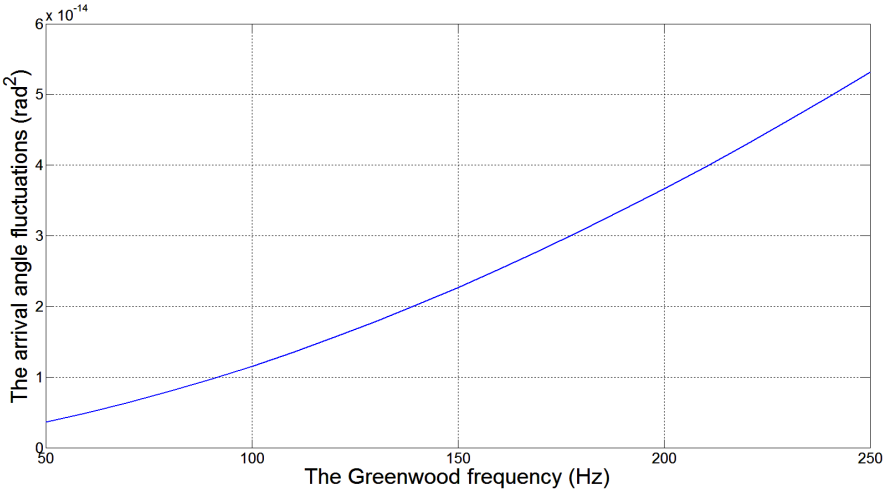

Fig. 2. The relationship between arrival angle fluctuation and GF.

#262563 Received 5 Apr 2016; revised 1 Jun 2016; accepted 2 Jun 2016; published 8 Jun 2016

Since the arrival fluctuations are caused by the fluctuations of the beam tilt, as illustrated in Fig. 2, with the increase of the GF, the variance of the arrival angle fluctuation gradually increases. However, in a practical CFSOC system, the arrival angle is usually less than 1 rad [16]. In a practical system, the ME is a time-variable, and the RMS value is used to evaluate the volatility of the ME. According to Eq. (14), the relationship between the RMS of the ME and the RMS of the tilt aberrations under different GF is shown in Fig. 3.

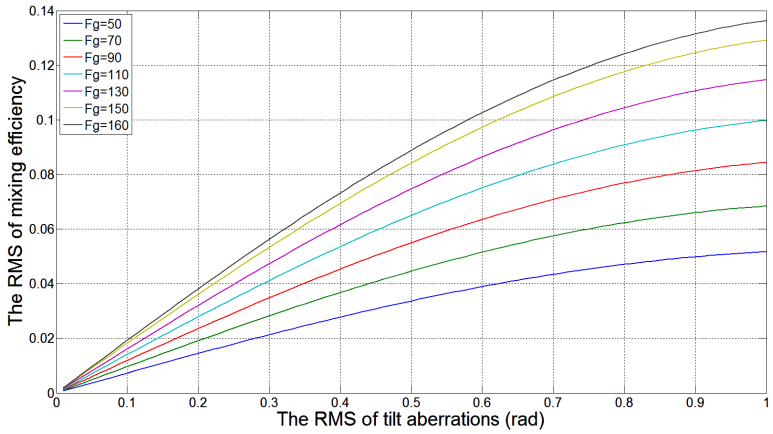

Fig. 3. The relationship between the RMS of the ME and tilt aberrations.

As shown in Fig. 3, the RMS of the ME is proportional to the RMS of the tilt aberrations under different GF. When the RMS of the tilt aberrations reaches 1 rad, all of the RMS of the ME under different GF grows more than 0.05. Especially, when the GF is more than 100 Hz, the RMS of the ME is more than 0.1. In addition, for the same RMS of the tilt aberrations, as the larger the GF grows up, the more RMS of ME will be. This is the influence of the time-domain characteristics of the turbulence.

Above all, the influence of GF on the arrival angle fluctuation and the RMS of ME is analyzed. According to Eq. (23), we can obtain the BER of CFSOC system easily. Next, we will discuss the influence of the high-order aberrations on the ME and BER of the CFSOC. Assuming the aberrations are composed of the high-order component, and a closed-loop AO unit is employed to correct high-order wavefront aberrations. According to Eq. (19), when d = 0.11 m, α_F = 0.28, r_0 = 0.1 m, and k = 0.5, the relationship between the ME and CLCB under different GF is obtain as shown in Fig. 4.

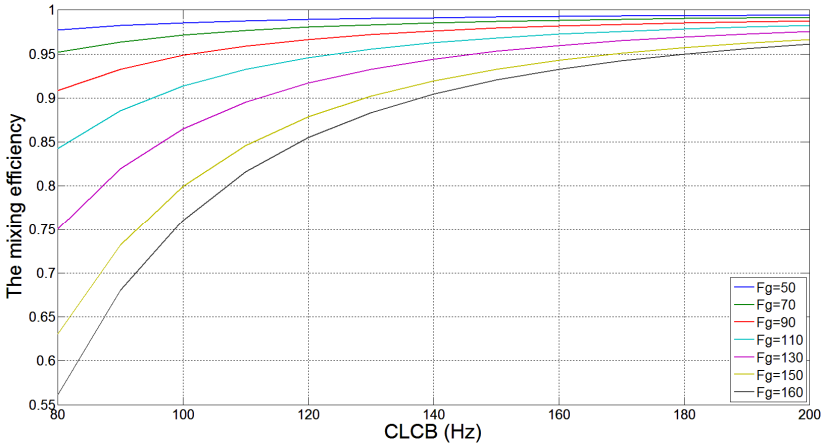

Fig. 4. The relationship between the CLCB and ME.

#262563 Received 5 Apr 2016; revised 1 Jun 2016; accepted 2 Jun 2016; published 8 Jun 2016

As Fig. 4 illustrates, under different GF, the greater the CLCB of the AO unit is, the higher the ME will be. For different GF, when the CLCB is above 100Hz, the ME can achieve above 0.75 under the different GF. When the CLCB increases to above 140Hz, the ME can reach to above 0.9. Thus, when the CLCB is nearly or more than the GF, the ME is more than 0.85. Similarly, according to Eq. (23), assuming D/r_0 is a constant, when $N_p = 10$, $\delta = 1$, the relationship between the CLCB and BER is shown in Fig. 5.

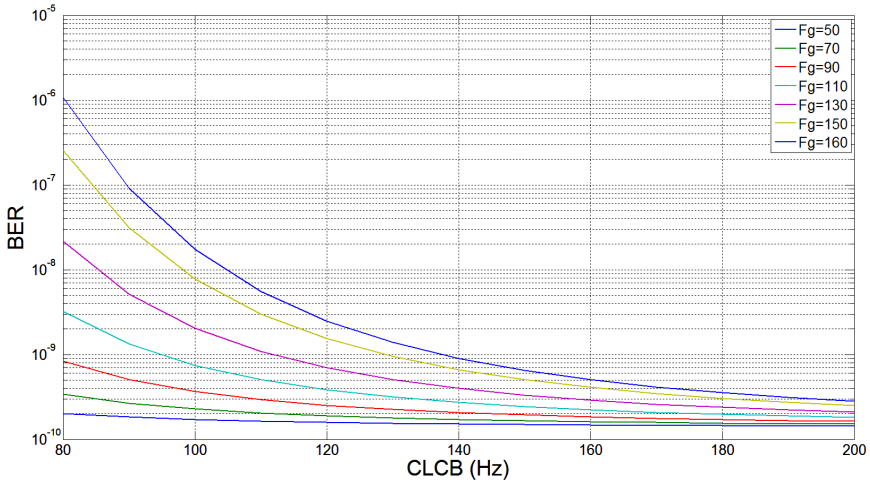

Fig. 5. The relationship between the CLCB and BER.

As shown in Fig. 5, when the GF is less than 90 Hz, the BER can be controlled to less than 10^{-9} with the CLCB is 80 Hz. When the GF is more than 90 Hz, the CLCB must increase to 100 Hz to meet the BER of less than 10^{-9}. When the GF is 160 Hz, the CLCB must be above 140 Hz to guarantee a BER below 10^{-9}. Thus, only the CLCB is nearly or more than the GF can the BER be below 10^{-9}.

Generally, the CLCB is limited by a control parameter, sampling frequency, and resonant frequency of the control system. Above all, for the CFSOC system with an AO unit, the temporal domain characteristics of atmospheric turbulence, such as the GF, severely influence communication performance.

4. Experiments and results analysis

4.1 The analysis of the tilt aberrations correction

In order to further analyze the impact of the GF on the performance of the CFSOC, an experimental system is designed by an AO unit with a double-stage FSM and a 97 element CSDM. This experimental system is designed to match an imaging telescope of a 1.2 m aperture. The wavelength of the laser is 532 nm. The Shack-Hartmann (S-H) wavefront sensor operates at 550 nm, since the unit of the residual aberrations measured by S-H wavefront sensor is wavelength, we can easily transform the residual aberrations data at 1550 nm to be consistent with the communication wavelength [16]. The schematic diagram of the experimental system is described in Fig. 6.

#262563 Received 5 Apr 2016; revised 1 Jun 2016; accepted 2 Jun 2016; published 8 Jun 2016

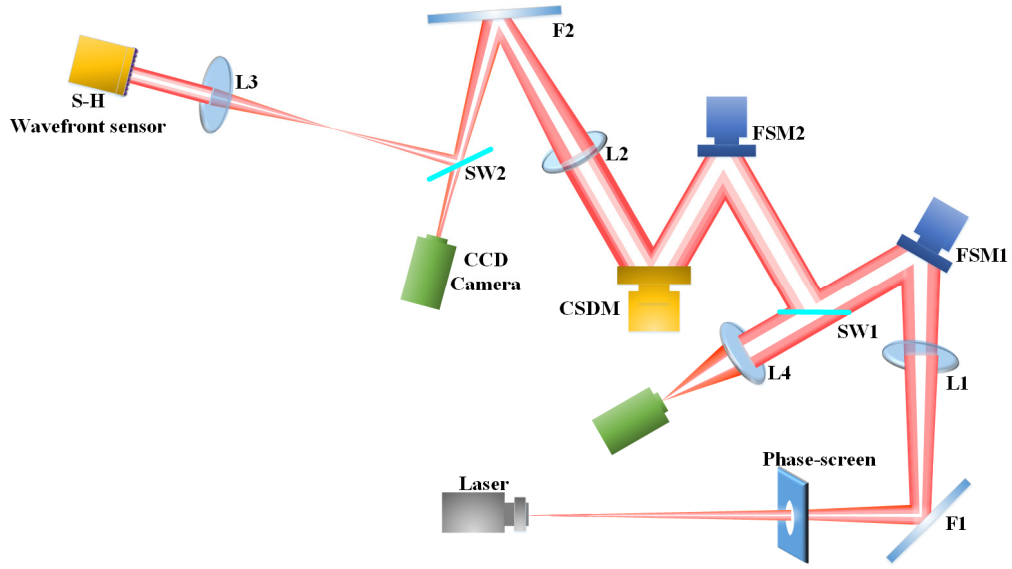

Fig. 6. The schematic diagram of experimental system.

As shown in Fig. 6, the laser beam is collimated through the phase-screen and L1, and then passes the double-stage FSM. The high-speed camera and the FSM1 are used to measure and correct the low-frequency tilt, the FSM2 is used to compensate the high-frequency tilt according to the tilt aberrations measured by S-H wavefront sensor. Then, the beam passes though the CSDM and is split into two parts. The one is imaged and the other is used to aberrations measurement. Thus, the AO unit is composed by the FSM1, the FSM2, the high-speed camera, the S-H wavefront sensor, and the CSDM which is used to correct the wavefront aberrations caused by atmospheric turbulence. Here the CSDM and the S-H wavefront sensor are conjugated in order to the best wavefront correction. And the phase-screen used in our experiment is customized by Lexitek corporation, the relative location between the laser and L1 determines the r_0 and the rotation speed determines the GF. In our experiment, we select the r_0 is 10 cm and change the GF though adjusting the rotation speed of the phase-screen.

In Fig. 6, the focal length of L1 and L3 is 400 mm and 3000 mm, respectively, and the aperture of L1 and L3 is 76 mm. The focal length of L2 and L4 is 3000 mm and 300 mm, respectively, and the aperture of L2 and L4 is 80 mm. The high speed and large stroke FSM made in the PI Corporation are chosen in the double-stage FSM unit separately. The first stage FSM uses a high-speed short wave infrared camera as the measuring camera, the maximum frame frequency can achieve 400 Hz, and the pixel size is 20 μm. The second-stage FMS is driven according to the tilt measured by the S-H wavefront sensor, and the high-speed camera with a frame frequency of 500 Hz is used as the wavefront sensor. The CSDM is used to correct the high-order aberrations, and the stroke of actuators is 5 μm. The number of the effective subapertures is 97. The aperture and focal length of microlens is 200 μm and 7 mm, respectively. The photo of the designed experimental system is shown in Fig. 7.

#262563 Received 5 Apr 2016; revised 1 Jun 2016; accepted 2 Jun 2016; published 8 Jun 2016

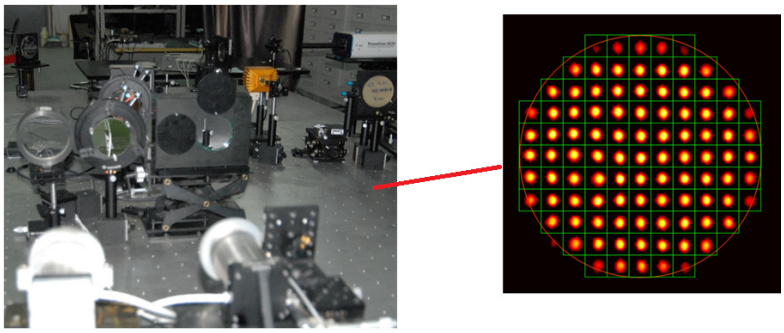

Fig. 7. The photo of experimental system.

Due to the double-stage FSM unit is used in our experiment, we analyze the ME and BER in the condition of using only the first-stage FSM, the double-stage FSM, and the high-order aberrations correction. In the following, we will analyze the performance of the arrival angles, BER, ME and its fluctuation with different GF (50 Hz, 100 Hz, and 160 Hz), and the results will be given.

When the GF is 50 Hz, the fluctuations of the arrival angles without tilt aberrations, with first-stage tilt correction and with double-stage tilt correction are shown in Fig. 8.

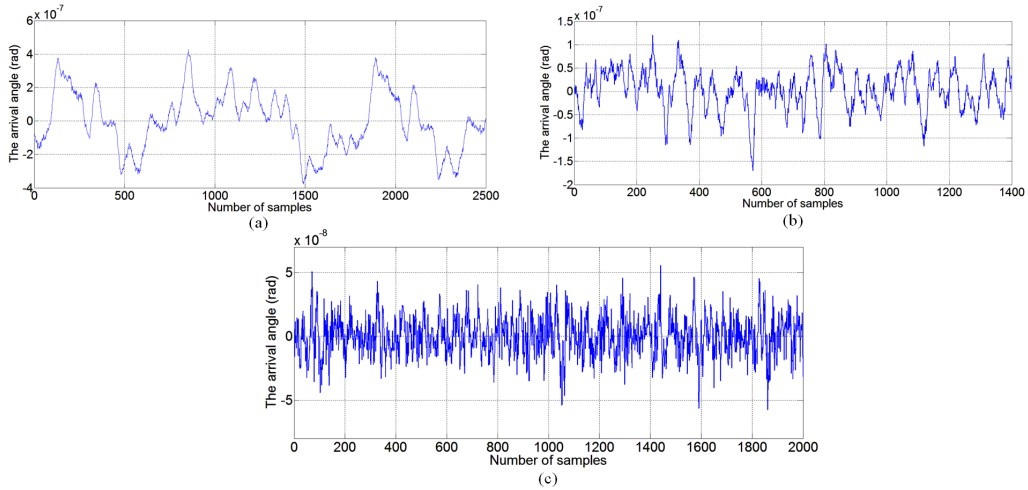

Fig. 8. The Results of the arrival angle when GF is 50 Hz, where (a) is without tilt correction (the variance is 2.988 × 10^{-14} rad^2), (b) is with first-stage FSM correction (the variance is 2.190 × 10^{-15} rad^2) and (c) is with double-stage FSM tilt correction (the variance is 2.363 × 10^{-16} rad^2).

As illustrated in Fig. 8, after only the first-stage FSM correction, the arrival angles can be reduced to one-third of that before correction. However, after double-stage FSM correction, the arrival angles can be decreased an order of magnitude. Hence, the double-stage FSM is able to reduce the arrival angles effectively. In the meanwhile, the first-stage tilt correction and the double-stage tilt correction are able to decrease the variance of the arrival angle fluctuations significantly.

As illustrated in Fig. 8, the arrival angle grows up significantly with the increase of the GF, and the results are consistent with numerical simulation results in Fig. 2. According to Eqs. (13) and (23), assuming $\delta = 1$ and $N_p = 10$, the results of the ME and BER when the GF is 50 Hz are shown in Table 1.

#262563 Received 5 Apr 2016; revised 1 Jun 2016; accepted 2 Jun 2016; published 8 Jun 2016

Table 1. Results of the ME and BER when the GF is 50 Hz.

Status	ME	BER
Without tilt correction	0.7589	1.797×10^{-8}
After first-stage tilt correction	0.9564	3.103×10^{-10}
After double-stage tilt correction	0.9951	1.403×10^{-10}

According to Table 1, we can conclude that the ME can be increased to more than 0.95 and the BER can be reduced to below 10^{-9} when the GF is 50 Hz, whether after only first-stage tilt correction or double-stage. Considering the ME is time variable, according to Eq. (14), the RMS of the tilt aberrations is related to the RMS of the ME. The RMS of the ME when the GF is 50 Hz is shown in Table 2.

Table 2. The fluctuations of the ME when the GF is 50 Hz.

Status	The RMS value of ME
Without tilt correction	0.04
After first-stage tilt correction	0.002
After double-stage tilt correction	0.0002

As shown in Table 2, since the change of the refractive-index structure constant is slow for the near ground horizontal-path transmission, the RMS of the ME is less than 0.1 with and without tilt corrections. However, after the first-stage FSM correction, the RMS is 0.002, and it further falls to 0.0002 after the double-stage FSM correction.

In the same way, when the GF is 100 Hz and 160 Hz, the results of the variance of the arrival angles, the ME, the BER and the fluctuation of the ME are shown as follows. The variance of the arrival angles under different GF is given in Table 3.

Table 3. The results of arrival angle fluctuations.

GF (Hz)	The variance of arrival angle fluctuations (rad^2) without tilt correction	The variance of arrival angle fluctuations (rad^2) with first-stage FSM	The variance of arrival angle fluctuations (rad^2) with double-stage FSM
50	2.988×10^{-14}	2.190×10^{-15}	2.363×10^{-16}
100	3.864×10^{-14}	5.344×10^{-15}	5.080×10^{-16}
160	4.792×10^{-14}	1.527×10^{-14}	1.348×10^{-15}

The Table 3 shows that all variance of arrival angle is less than 10^{-15} after double-stage tilt correction. However, the effect of the correction when GF is 160 Hz is worse than the other two. The results of the ME under different GF are shown in Table 4.

Table 4. The results of the ME under different GF.

GF (Hz)	The ME without tilt correction	The ME with first-stage FSM	The ME with double-stage FSM
50	0.7589	0.9564	0.9951
100	0.7130	0.9386	0.9915
160	0.6435	0.8422	0.9774

According to Eq. (23), N_p is the description of the detected photons per bit. For CFSOC system with BPSK modulation, we select $N_p = 10$, $N_p = 15$ and $N_p = 20$. Thus, assuming $\delta = 1$, the results of the BER under different GF and N_p are shown in Table 5.

#262563 Received 5 Apr 2016; revised 1 Jun 2016; accepted 2 Jun 2016; published 8 Jun 2016

Table 5. The results of the BER under different GF and N_p.

GF (Hz)	N_p	The BER without tilt correction	The BER with first-stage FSM	The BER with double-stage FSM
50	10	1.797×10^{-8}	3.103×10^{-10}	1.403×10^{-10}
50	15	7.492×10^{-12}	1.794×10^{-14}	5.508×10^{-15}
50	20	3.299×10^{-15}	1.096×10^{-18}	2.283×10^{-19}
100	10	4.641×10^{-8}	4.467×10^{-10}	1.510×10^{-10}
100	15	3.067×10^{-11}	3.084×10^{-14}	6.140×10^{-15}
100	20	2.139×10^{-14}	2.249×10^{-18}	2.638×10^{-19}
160	10	1.955×10^{-7}	3.2381×10^{-9}	2.015×10^{-10}
160	15	2.591×10^{-10}	5.870×10^{-13}	9.434×10^{-15}
160	20	3.622×10^{-13}	1.124×10^{-16}	4.667×10^{-19}

According to Table 4 and Table 5, when $N_p = 10$, the ME is up to 0.9 and the BER falls to below 10^{-9} when the GF is 50 Hz and 100 Hz, whether after first-stage or double-stage tilt correction. However, when the GF is 160 Hz, the ME after the first-stage tilt correction is only about 0.85 and the BER just reaches 10^{-9}. After double-stage tilt correction, the ME can increase to above 0.95 and the BER is able to decrease to 10^{-10} when the GF is 160 Hz. Thus, the double-stage is necessary to guarantee the low BER. For the condition of $N_p = 15$ and $N_p = 20$, the results without and with double-stage tilt correction are all below 10^{-9}. Especially, when GF is 160 Hz, the performance improvement is more effectively. In the same way, the RMS of the ME is analyzed under different GF, and the results are shown in Table 6.

Table 6. The results of the RMS of the ME.

GF (Hz)	The RMS value of the ME without tilt correction	The RMS value of the ME with first-stage FSM	The RMS value of the ME with double-stage FSM
50	0.04	0.002	0.0002
100	0.06	0.009	0.0007
160	0.08	0.02	0.002

According to Table 6, the fluctuation of the ME becomes larger with the increase of the GF, whether after first-stage or double-stage tilt corrections. However, the effect of the correction is significant enough.

4.2 The analysis of the high-order aberrations correction

In this section, we will analyze the influence of high-order aberrations on the performance of a CFSOC system. The aberrations are only composed of high-order aberrations, described with above the 4th item Zernike polynomials. In our experiment, we set r_0 as 10 cm, the mean value and the RMS of the ME without high-order aberrations correction under the GF is 50 Hz, GF is 100 Hz, and GF is 160 Hz is obtained as shown in Table 7.

Table 7. The mean value and RMS of the ME without high-order aberrations correction.

GF (Hz)	The mean value	The RMS value
50	0.15	0.10
100	0.17	0.15
160	0.18	0.16

As shown in Table 7, the mean and RMS values show a little increase as the GF increasing, however, the fluctuation frequency increases obviously with the GF increasing. Similarly, according to Eq. (23), when $\delta = 1$, $N_p = 10$, the mean value and RMS of the BER without high-order aberrations correction under the GF is 50 Hz, 100 Hz, and 160 Hz is shown in Table 8.

#262563 Received 5 Apr 2016; revised 1 Jun 2016; accepted 2 Jun 2016; published 8 Jun 2016

Table 8. The mean value and RMS of the BER without high-order aberrations correction.

GF (Hz)	The mean value	The RMS value
50	2.70×10^{-2}	0.048
100	2.84×10^{-2}	0.052
160	3.10×10^{-2}	0.061

Similarly, the mean value and RMS of the ME after closed-loop correction under the GF is 50 Hz, 100 Hz and 160 Hz are illustrated in Table 9.

Table 9. The mean value and RMS of the ME after correction (CLCB is 100 Hz).

GF (Hz)	The mean value	The RMS value
50	0.998	0.0007
100	0.908	0.0045
160	0.694	0.0089

According to Table 9, we note that the ME can reach above 0.9 after high-order aberrations correction when the GF is 50 Hz and 100 Hz. However, when the GF is 160 Hz, the ME is only about 0.7 after correction. The reason is that the CLCB is only about 100 Hz, which cannot retrain the high-frequency atmospheric turbulence effectively. These results are consistent with the numerical simulation shown in Fig. 4.

Selecting $\delta = 1$, N_p = 10, according to Eq. (23), the BER after closed-loop correction is able to be calculated when the GF is 50 Hz, 100 Hz, and 160 Hz, and the results of the mean value and RMS of the BER after closed-loop correction when the CLCB is 100 Hz are shown in Table 10.

Table 10. The mean value and RMS of the BER after correction (CLCB is 100 Hz).

GF (Hz)	The mean value	The RMS value
50	1.32×10^{-10}	1.99×10^{-12}
100	8.45×10^{-10}	8.01×10^{-11}
160	6.96×10^{-8}	1.37×10^{-8}

According to Table 10, when the GF is 50 Hz and 100 Hz, the BER is decreased to below 10^{-9} after closed-loop correction. While, due to the limitation of the CLCB, when the GF is 160 Hz, the BER is only near to 10^{-8} after closed-loop correction.

In order to improve the performance of the CFSOC system even more when the GF is 160 Hz, we increase the CLCB to 120 Hz through improving the sampling frequency, ME, and BER after closed-loop correction shown in Table 11.

Table 11. The results of the ME and BER after correction (CLCB is 120 Hz).

GF (Hz)	The mean value of ME	The mean value of BER	The RMS value of ME	The RME value of BER
160	0.830	4.18×10^{-9}	0.006	5.35×10^{-10}

As shown in Table 11, when the CLCB is 120 Hz and the GF is 160 Hz, the ME grows up to more than 0.8, and the BER is decreased to nearly 10^{-9}. Limited to the sample frequency, resonant frequency of the execution unit, and other factors, the CLCB cannot be further increased.

5. Discussion and conclusion

The influence of the GF on the performance of CFSOC is studied with and without tilt and high-order aberrations correction, and the relationship between the fluctuation of the arrival angle, the high-order wavefront aberrations, and the GF is derived. The performance of the BER, ME, and its fluctuation is analyzed in detail according to the experimental data. These results will contribute to the analysis and design of AO unit for CFSOC.

The experimental results show that the higher CLCB is necessary to guarantee communication quality with the increase of the GF, whether only considering the tilt or high-order aberrations. When considering the aberrations are only tilt, the double-stage FSM unit is

#262563 Received 5 Apr 2016; revised 1 Jun 2016; accepted 2 Jun 2016; published 8 Jun 2016

an effective way to increase the CLCB. In our experiment, when the GF is 160 Hz, the BER is able to fall to below 10^{-9} with the double-stage FSM unit. Similarly, when considering the aberrations are only high-order components, with an increase of the GF, the low CLCB degrades the closed-loop correction performance of the AO unit. Limited by the low CLCB (120 Hz), when the GF is 160 Hz, the BER can only reach 10^{-9}. Comparing to the results of considering tilt and high-order aberrations, the CLCB of the correction considering only tilt is high enough to guarantee the BER below 10^{-9}. However, for high-order aberrations correction, the CLCB of the AO unit is such low to effectively compensate the high-order wavefront distortions that the BER is not able to achieve below 10^{-9}.

Thus, the high-order components can be compensated further by improving the CLCB through increasing sampling and the resonant frequency. And an experimental CFSOC system with an AO unit will be building and the ME and BER will be measuring by special instruments in the future work.

Acknowledgments

The authors acknowledge helpful suggestions from the reviewers and help from the editors. This work was supported by National 863 Plan Project (2013AA063903) and China Postdoctoral Science Foundation (2016M590255).

#262563 Received 5 Apr 2016; revised 1 Jun 2016; accepted 2 Jun 2016; published 8 Jun 2016